

Strong Lensing Mass of a Galaxy Cluster Discovered by the Planck Satellite [★]

Cristóbal Sifón,^{1,3,6} Felipe Menanteau,^{2,6} John P. Hughes,^{2,6} Mauricio Carrasco^{3,4,5} and L. Felipe Barrientos³

¹ Leiden Observatory, Leiden University, PO Box 9513, NL-2300 RA Leiden, Netherlands

² Rutgers University, Department of Physics & Astronomy, 136 Frelinghuysen Rd, Piscataway, NJ 08854, USA

³ Departamento de Astronomía y Astrofísica, Facultad de Física, Pontificia Universidad Católica de Chile, Casilla 306, Santiago 22, Chile

⁴ Zentrum für Astronomie, Institut für Theoretische Astrophysik, Albert-Überle Straße 2, 69120 Heidelberg, Germany

⁵ European Southern Observatory, Alonso de Córdova 3107, Vitacura, Santiago, Chile

Preprint online version: March 21, 2022

ABSTRACT

Context. The recent discovery of a large number of galaxy clusters using the Sunyaev-Zel'dovich (SZ) effect has opened a new era on the study of the most massive clusters in the Universe. Multi-wavelength analyses are required to understand the properties of these new sets of clusters, which are a sensitive probe of cosmology.

Aims. We aim at a multi-wavelength characterization of PLCK G004.5–19.5, one of the most massive X-ray validated SZ effect-selected galaxy clusters discovered by the *Planck* satellite.

Methods. We have observed PLCK G004.5–19.5 with GMOS on the 8.1m-Gemini South Telescope for optical imaging and spectroscopy, and performed a strong lensing analysis. We also searched for associated radio emission in published catalogs.

Results. An analysis of the optical images confirms that this is a massive cluster, with a dominant central galaxy (the BCG) and an accompanying red sequence of galaxies, plus many strongly lensed background galaxies including a 14''-long arc. Longslit spectroscopy of 6 cluster members shows that the cluster is at $z = 0.516 \pm 0.002$. We also targeted the most prominent lensed galaxy, and found $z_{\text{arc}} = 1.601$. From a strong lensing analysis we measure a median Einstein radius $\theta_E \simeq 29''$ and estimate an enclosed mass $M_E = (2.38 \pm 0.55) \times 10^{14} M_\odot$. By extrapolating an NFW profile we find a total mass $M_{500}^{SL} = 6.1_{-1.2}^{+2.3} \times 10^{14} M_\odot$. This mass is considerably lower than that implied by the SZ and X-ray observations, which may indicate a departure from the NFW profile for PLCK G004.5–19.5. The analysis of archival radio data at 843 MHz and 1.4 GHz suggest that PLCK G004.5–19.5 hosts a powerful radio relic on scales $\lesssim 1$ Mpc.

Key words. Cosmology: Observations: Galaxy Clusters: Individual: PLCK G004.5–19.5 – Gravitational Lensing: Strong

1. Introduction

In the last few years, the Sunyaev-Zel'dovich (SZ) effect has proven to be an effective method to find massive galaxy clusters at all redshifts, with results from the Atacama Cosmology Telescope (ACT, e.g., [Marriage et al. 2011](#); [Hasselfield et al. 2013](#)), the South Pole Telescope (SPT, e.g., [Williamson et al. 2011](#); [Reichardt et al. 2013](#)) and the *Planck* satellite (e.g., [Planck Collaboration 2011a, 2013](#)) already yielding a few hundred newly discovered clusters up to $z \sim 1.4$. The SZ effect is a distortion in the Cosmic Microwave Background (CMB) spectrum in the direction of galaxy clusters caused by inverse Compton scattering of CMB photons by the hot electrons in the intracluster gas ([Sunyaev & Zel'dovich 1972](#)). Multi-wavelength follow-up observations of SZ-selected clusters have confirmed the unique potential of the SZ effect for detecting the most massive clusters

in the Universe (e.g., [Sifón et al. 2012](#); [Benson et al. 2013](#)), with the SZ-discovered El Gordo and SPT-CL J2344–4243 being two of the most extreme galaxy clusters ever known ([Menanteau et al. 2012](#); [McDonald et al. 2012](#)). As expected, many of these clusters display strong lensing features ([Menanteau et al. 2010a](#)), a good indication that these are very massive systems.

Observations of these strongly lensed background galaxies offer one of the most robust ways of constraining the mass of a cluster, providing a direct measure of the mass within the Einstein radius (see [Kneib & Natarajan 2011](#), for a recent review). In combination with other probes (such as X-rays and weak lensing), strong lensing analyses have provided some of the most complete mass distribution models for galaxy clusters, even allowing for the determination of the 3-dimensional configuration in some cases (e.g., [Morandi et al. 2010](#); [Limousin et al. 2012](#)).

Here, we present optical confirmation and a strong lensing analysis of PLCK G004.5–19.5, one of the most massive, hot and X-ray luminous galaxy clusters discovered by the *Planck* satellite via the SZ effect and validated with *XMM-Newton* X-ray observations ([Planck Collaboration 2011b](#)). Additionally, we show from archival radio imaging that PLCK G004.5–19.5 likely hosts a powerful radio relic, extended on scales $\lesssim 1$ Mpc.

All uncertainties are quoted at the 68.3% (1σ) confidence level. We assume a flat Λ CDM cosmology with $\Omega_M = 0.3$ and

[★] Based on observations obtained at the Gemini Observatory, which is operated by the Association of Universities for Research in Astronomy, Inc., under a cooperative agreement with the NSF on behalf of the Gemini partnership: the National Science Foundation (United States), the Science and Technology Facilities Council (United Kingdom), the National Research Council (Canada), CONICYT (Chile), the Australian Research Council (Australia), Ministério da Ciência, Tecnologia e Inovação (Brazil) and Ministerio de Ciencia, Tecnología e Innovación Productiva (Argentina)

⁶ Visiting astronomer, Gemini South Observatory

$H_0 = 70 \text{ km s}^{-1} \text{ Mpc}^{-1}$. Masses and other quantities are reported within a radius r_{500} , which encloses a mean density 500 times the critical density of the Universe at the corresponding redshift. All quantities reported by [Planck Collaboration \(2011b\)](#) have been corrected to the spectroscopic redshift $z = 0.516$.

2. Observations and Data Analysis

2.1. SZ and X-ray Data

PLCK G004.5–19.5 was discovered through its SZ effect by the *Planck* satellite. With a signal-to-noise ratio (S/N) of 5.9 in the Early Science release, it is just below the S/N threshold of 6.0 set for the *Planck* Early SZ sample ([Planck Collaboration 2011a](#))¹. Despite this relatively low S/N, it has a strong integrated SZ signal, $Y_{500} = (1.90 \pm 0.19) \times 10^{-4} \text{ Mpc}^2$, where $Y \equiv \int y d\Omega$. Here, y is the usual Compton parameter and the integral is over the solid angle of the cluster. We use the $Y - M$ scaling relation of [Planck Collaboration \(2011c\)](#) to estimate a mass $M_{500}^{\text{SZ}} = (10.4 \pm 0.7) \times 10^{14} M_{\odot}$.

PLCK G004.5–19.5 was subsequently validated using *XMM-Newton* ([Planck Collaboration 2011b](#)), which confirmed that it is an extended X-ray source. Moreover, the observed energy of the Fe K emission line allowed a redshift determination $z_{\text{Fe}} = 0.54$, making it the highest-redshift cluster of the initial *Planck*–*XMM-Newton* validation program. The X-ray analysis of [Planck Collaboration \(2011b\)](#) proves that PLCK G004.5–19.5 is a hot, massive cluster, with an X-ray luminosity² (in the [0.1–2.4] keV band) of $L_X = 1.6 \times 10^{45} \text{ erg s}^{-1}$, an integrated temperature $kT_X = 10.2 \pm 0.5 \text{ keV}$ and a gas mass $M_{\text{gas}} = 1.3 \times 10^{14} M_{\odot}$. Combined, the latter two give a pseudo-Compton parameter $Y_X \equiv kT_X M_{\text{gas}} = (13.3 \pm 0.9) \times 10^{14} M_{\odot} \text{ keV}$. With this latter value, [Planck Collaboration \(2011b\)](#) estimate a total mass $M_{500}^X = (9.6 \pm 0.5) \times 10^{14} M_{\odot}$.

2.2. Optical Imaging

PLCK G004.5–19.5 was observed on UT 2012 July 19 with the *gri* filters with GMOS on the Gemini-South Telescope (ObsID:GS-2012A-C-1, PI:Menanteau), with exposure times of $8 \times 60 \text{ s}$, $8 \times 90 \text{ s}$ and $8 \times 150 \text{ s}$ respectively. Observations were performed with photometric conditions and seeing $\sim 0.''6$. Images were coadded using SWarp ([Bertin et al. 2002](#)) and photometry was performed using SExtractor ([Bertin & Arnouts 1996](#)) in dual mode, using the *i*-band for detection. Figure 1 shows the combined *gri* image³ of PLCK G004.5–19.5, which shows clearly that there is an overdensity of red elliptical galaxies with a central dominant Brightest Cluster Galaxy (BCG) close to the X-ray peak. Figure 1 also reveals the presence of several strong lensing features, most notably a giant arc to the West of the BCG, roughly $14''$ long.

Each galaxy is assigned a photometric redshift by fitting Spectral Energy Distributions (SEDs) to the *gri* photometry using the BPZ code ([Benítez 2000](#)) including correction for galactic extinction as described in [Menanteau et al. \(2010a,b\)](#). Typical uncertainties are $\delta z/(1+z) \approx 0.09$. The photometric redshift of the cluster, $z_{\text{phot}} = 0.51 \pm 0.02$, was estimated as in [Menanteau](#)

¹ PLCK G004.5–19.5 has been included in the new *Planck* SZ catalog ([Planck Collaboration 2013](#)) with a S/N of 6.15.

² The uncertainties in the X-ray values from [Planck Collaboration \(2011b\)](#) do not include systematic errors and have been dropped when negligible.

³ Created with STIFF ([Bertin 2012](#)).

Table 1. Spectroscopically confirmed cluster members.

ID	RA (hh:mm:ss)	Dec (dd:mm:ss)	<i>i</i> mag. (AB mag)	Redshift ^a
1 ^b	19:17:05.08	−33:31:20.6	18.47	0.5199 ± 0.0005
2	19:17:07.80	−33:31:31.2	19.74	0.5126 ± 0.0005
3	19:17:08.98	−33:31:48.4	19.16	0.5074 ± 0.0004
4	19:17:09.49	−33:31:43.5	19.70	0.5150 ± 0.0003
5	19:17:10.20	−33:31:38.5	19.83	0.5176 ± 0.0003
6	19:17:14.40	−33:31:57.5	20.48	0.5187 ± 0.0002

^(a) Errors as given by RVSAO.

^(b) Brightest Cluster Galaxy.

[et al. \(2010a,b\)](#) and is consistent with the spectroscopic redshift (Sec. 2.3). We consider as cluster members all galaxies within $\Delta z = 0.03(1+z_0) = 0.045$ of $z_0 = 0.51$ and brighter than $m^* + 2 \approx 22.9$ in the *i*-band, for a total 222 photometrically-selected members. (Here m^* is the characteristic luminosity of the [Schecter \(1976\)](#) function as found by [Blanton et al. \(2003\)](#), passively evolved to z_0 .)

2.3. Optical Spectroscopy

We performed longslit spectroscopy of PLCK G004.5–19.5 on UT 2012 July 20 with GMOS, with $0.''75$ -wide slits with three pointings, two aimed at confirming cluster members and one targeting the most prominent strongly lensed background galaxy. The data were reduced using PyGMOS⁴ ([Sifón et al. 2012](#)), with an average wavelength calibration root-mean-square (rms) uncertainty of 0.4 \AA . Redshifts were measured by cross-correlating the spectra with Sloan Digital Sky Survey ([Abazajian et al. 2009](#)) template spectra using the IRAF package RVSAO ([Kurtz & Mink 1998](#)). The six confirmed cluster members are listed in Table 1 and are shown in Figure 1 by green circles. They are all red, passive elliptical galaxies and have a rest-frame velocity dispersion $\sigma \sim 860 \text{ km s}^{-1}$ (which is likely not representative of the cluster velocity dispersion). The median redshift of these 6 members, $z = 0.516 \pm 0.002$, is adopted as the cluster redshift (with uncertainties given by $\sigma \sqrt{\pi/2N}$).

The left panel of Figure 2 shows a zoomed-in view of the brightest lensed galaxy. Two brightness peaks can be identified, which we interpret as two blended strong lensing images of a single source (see Sec. 3). The top-right panel shows the 2d spectrum along the arc, where a faint continuum can be distinguished between the north and south images. The red inset histogram shows the normalized counts for each row over the spectral range shown, after an iterative 3σ -clipping rejection so that bad pixels and emission lines are not included in the counts. This histogram shows that the decrease in brightness is significant between the two peaks but that this region is, in turn, still detected at high significance. The middle- and bottom-right panels show the 1d spectra of the two brightness peaks. Both spectra clearly show 5 redshifted FeII absorption lines with rest-frame wavelengths 2344.2, 2374.5, 2382.8, 2586.6 and 2600.2 Å. The median redshift of these 5 pairs of lines is $z_{\text{arc}} = 1.6008 \pm 0.0002$. The bottom spectrum also shows three emission lines (seen in the 2d spectrum as well), which correspond to H β and [OIII] $\lambda\lambda 4958, 5007 \text{ \AA}$ from a foreground compact star-forming galaxy at $z = 0.203$, for which H α emission is also observed but not shown in Figure 2.

⁴ <http://www.strw.leidenuniv.nl/~sifon/pygmos/>

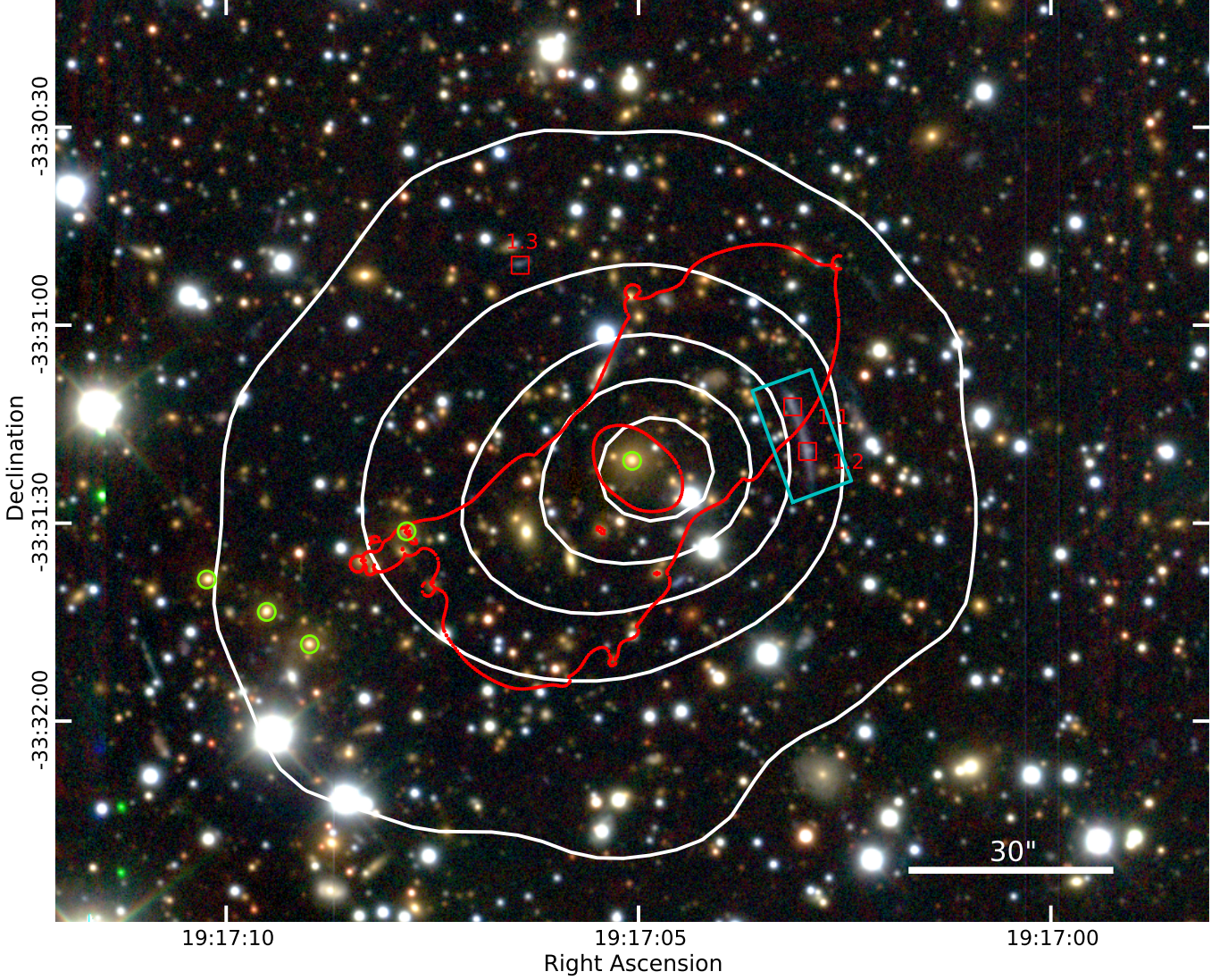


Fig. 1. GMOS *gri* pseudo-color image of the central region of PLCK G004.5–19.5. North is up, east is left. X-ray surface brightness contours from *XMM-Newton* are overlaid in white. Spectroscopic cluster members are marked by green circles; only 5 out of 6 are visible in the shown region, the sixth member is to the SW of this region. Red squares mark the position of the 3 confirmed multiple images, while we show in red the critical curve for $z_s = 1.6$. The cyan box shows the region that has been zoomed-in in the left panel of Figure 2. The thick white line in the bottom right shows a $30''$ scale, corresponding to 188 kpc at $z = 0.516$.

3. Strong Lensing Analysis

The strong lensing analysis was performed using the Markov Chain Monte Carlo (MCMC) code `LENSTOOL` (Kneib 1993; Jullo et al. 2007), as follows. The cluster is modelled with an ellipsoidal Navarro-Frenk-White (NFW, Navarro et al. 1995) profile for the main halo, plus truncated Pseudo-Isothermal Elliptical Mass Distribution (PIEMD, Kassiola & Kovner 1993; Kneib et al. 1996) with a constant mass-to-light ratio for the 222 brightest cluster members (see Sec. 2.2). A PIEMD halo is modelled by three parameters: the core radius, r_{core} , the size of the halo (the cut-off radius), r_{cut} , and the velocity dispersion, σ_0 , which scale with galaxy luminosity as (Jullo et al. 2007):

$$r_{\text{core}} = r_{\text{core}}^* (L/L^*)^{1/2} \quad (1a)$$

$$r_{\text{cut}} = r_{\text{cut}}^* (L/L^*)^{1/2} \quad (1b)$$

$$\sigma_0 = \sigma_0^* (L/L^*)^{1/4}, \quad (1c)$$

where $L^* = 6.6 \times 10^{10} L_{\odot}$. The total mass of the galaxy is then given by

$$M = (\pi/G) (\sigma_0^*)^2 r_{\text{cut}}^* (L/L^*). \quad (2)$$

We fix $r_{\text{core}}^* = 0.3$ kpc, and r_{cut}^* and σ_0^* are free parameters. Therefore the mass model has eight free parameters: six for the main NFW halo and two for the PIEMD halos (see Table 2).

As can be seen in the red histogram of Figure 2, there is a decrease in brightness in the middle of the arc in between two prominent brightness peaks. We interpret this as the merging of two images of the background galaxy. We use this double-imaged arc with $z_{\text{arc}} = 1.6$ as a constraint for the lens model, and identify a third image of the same source to the North-East of the BCG (labelled 1.3 in Figure 1).

The total mass model is therefore optimized using the 222 brightest members (including the six spectroscopic members) and the three images for the background galaxy at $z = 1.601$. We adopt a positional uncertainty $\Delta \mathbf{x} = 1.74$ for the multiple images.

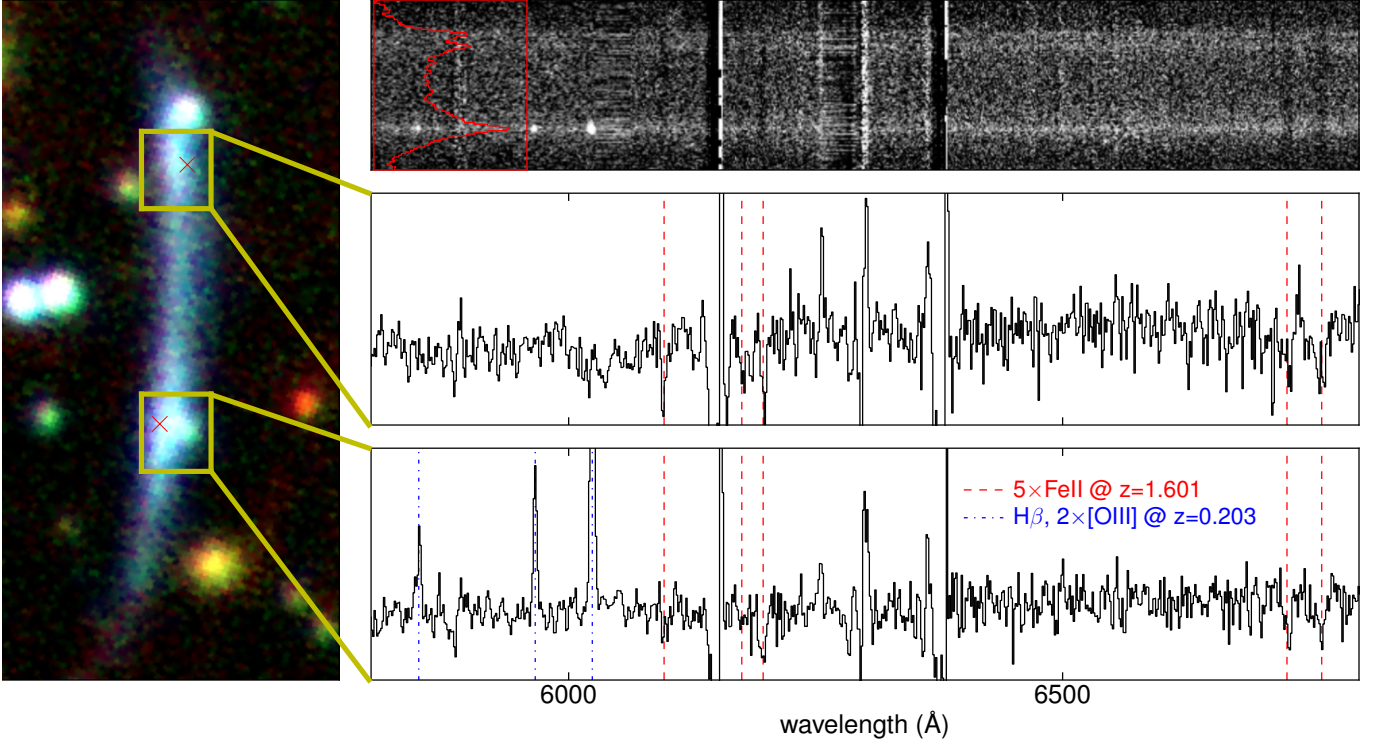


Fig. 2. The giant arc. The left panel shows a close-up *gri* image of the arc (cyan box in Figure 1), with the red crosses marking the location where LENS_{TOOL} predicts the images to be. The top right panel shows the GMOS 2d spectrum of the arc. The red histogram (inset) shows the total counts in each row over the shown spectral range, after an iterative 3σ -clipping to remove bad pixels and emission lines. This highlights the decrease in brightness (and the significance of the continuum) between the two images. The middle and bottom panels show, respectively, the 1d spectra of the northern (source 1.1) and southern (source 1.2) peaks seen in the lensed arc, each marked by a yellow square in the left panel. In these, the red dashed lines mark the 5 FeII absorption lines at $z = 1.601$ and the blue dash-dotted lines mark the emission lines from a foreground galaxy at $z = 0.203$, only seen in the south spectrum. The vertical axes in these two panels are in arbitrary units.

The goodness-of-fit for the best model is $\chi^2_{\text{red}}/\text{d.o.f.} = 0.15$, with a rms error on the image positions of $0.''22$. The total mass distribution is moderately elongated along the plane of the sky, approximately aligned with the light distribution. The best-fit values for the eight free parameters are listed in Table 2. The prior ranges are restricted, given the low number of constraints, to avoid any parameter drifting away due to degeneracies. In any case, errors are large enough that increasing the ranges gives consistent results in most cases. Note that the given priors act as initial information and do not limit the region that the MCMC can explore (e.g., the upper 68% uncertainty on the ellipticity is outside this range). Moreover, the mass within the Einstein ring itself (see below) is stable to changes in the model parameters.

Following Meneghetti et al. (2011), the Einstein radius is estimated as the median distance of the tangential critical curves to the cluster center. We find $\theta_E(z_s = 1.6) \approx 29''$, corresponding to a physical distance $r_E \approx 185$ kpc. Assuming a symmetric lens, the mass inside this region is $M_E = (2.38 \pm 0.55) \times 10^{14} M_\odot$. Integrating the 3-dimensional NFW profile for the main halo, we obtain $M_{500}^{SL} = 6.1^{+2.3}_{-1.2} \times 10^{14} M_\odot$. The mass integrated along the line of sight within r_{500} is, on the other hand, $M_{500}^{\text{los}} = (7.7 \pm 2.5) \times 10^{14} M_\odot$, where $r_{500} = 1.01^{+0.16}_{-0.08}$ Mpc is calculated from M_{500}^{SL} assuming a spherical cluster. We note that the values at r_{500} are an extrapolation of the data.

Recently, Zitrin et al. (2012) derived a representative distribution of Einstein radii from a sample of $\sim 10,000$ clusters

from the SDSS optically-selected sample of Hao et al. (2010). They found a log-normal Einstein radius distribution with mean and standard deviation $\langle \log(\theta_E^{\text{eq}}/\text{arcsec}) \rangle = 0.73 \pm 0.32$ for background sources at $z_s \sim 2$. For comparison to this work and others, we estimate the equivalent Einstein radius to be $\theta_E^{\text{eq}}(z_s = 1.6) \approx 25''$. PLCK G004.5–19.5 is a 2σ outlier from this mean relation; therefore it can be said to be within the 5% strongest lensing clusters in the Universe.

4. Radio Emission

Radio relics and radio halos are diffuse, non-thermal emission features that have no obvious connection with individual cluster galaxies and are often associated with merging activity in massive clusters of galaxies (see Feretti et al. 2012, for a recent review). We used VizieR⁵ (Ochsenbein et al. 2000) to search for such radio features around PLCK G004.5–19.5 on archival data. Figure 3 shows the intensity map at 1.4 GHz from the NRAO VLA Sky Survey (NVSS; Condon et al. 1998) with green contours, and red contours from the Sydney University Molonglo Sky Survey (SUMSS; Mauch et al. 2003) at 843 MHz. Both sets of contours are shown at 3, 5, 10 and 20 times each map’s background rms noise. Significant emission around PLCK G004.5–19.5 at both frequencies (clearly extended at 1.4 GHz) suggest that it hosts a powerful radio relic. At the 5σ

⁵ <http://vizier.u-strasbg.fr/viz-bin/VizieR>

Table 3. Radio Sources

Source ^a	Name	RA ^b (hh:mm:ss)	Dec ^b (dd:mm:ss)	F_ν ^c (mJy)	Size ^d (" × ")	P.A. ^e (deg)	α^f	$P_{1.4}$ (10^{25} W Hz ⁻¹)
A	NVSS J191715–332722	19:17:15.89(05)	–33:27:22.2(0.7)	34.9 ± 1.1	47 × 45	176	1.3	20
	SUMSS J191715–332720	19:17:15.75(11)	–33:27:20.6(2.0)	67.8 ± 2.7	73 × 49	165		
B	NVSS J191701–333035	19:17:01.75(08)	–33:30:35.6(1.3)	31.4 ± 1.5	74 × 51	33	0.9	18
	SUMSS J191701–333033	19:17:01.50(16)	–33:30:33.7(2.5)	49.3 ± 2.0	70 × 63	44		
C	NVSS J191710–333144	19:17:10.90(28)	–33:31:44.7(3.3)	4.8 ± 0.5	74 × 55	102	1.1	2
	SUMSS J191710–333139 ^g	19:17:10.55(37)	–33:31:39.0(4.6)	8.6 ± 1.4	57 × 52	3		
D	NVSS J191705–333333	19:17:05.94(32)	–33:33:33.6(8.0)	4.8 ± 0.6	81 × 49	173	1	3
E	NVSS J191717–333224	19:17:17.84(52)	–33:32:24.4(5.7)	3.4 ± 0.5	57 × 42	132	1	1

^(a) Sources ordered by signal-to-noise ratio in the NVSS catalog.

^(b) Nominal uncertainties on the last two digits in parentheses.

^(c) Integrated flux at 1.4 GHz for NVSS (rest-frame 2.12 GHz) and 833 MHz for SUMSS (rest-frame 1.28 GHz).

^(d) Major and minor axes, estimated using `IMFIT` within CASA.

^(e) Position angle West of North, estimated using `IMFIT` within CASA.

^(f) Spectral index, where $F(\nu) = \nu^{-\alpha}$. A spectral index of $\alpha = 1$ has been assumed for sources D and E.

^(g) Not in the SUMSS catalog; all parameters estimated by us using `IMFIT` within CASA.

Table 2. Best-fit parameters of the strong lensing model.

Parameter	Symbol	Prior ^a	Value	units
Main NFW Halo				
RA offset ^b	ΔRA	[–1.5,1.5]	$0.6^{+0.5}_{-1.4}$	arcsec
Dec offset ^b	ΔDec	[–1.5,1.5]	$-1.4^{+1.3}_{-0.5}$	arcsec
Ellipticity	e	[0.05,0.4]	$0.37^{+0.12}_{-0.05}$	
Position Angle ^c	θ	[40,60]	$49.8^{+4.9}_{-2.2}$	deg
Scale radius	r_s	[150,550]	158^{+173}_{-7}	kpc
Concentration ^d	c_{200}	[3,15]	$9.9^{+3.8}_{-0.3}$	
PIEMD Halos				
Cut-off radius	r_{cut}^*	[10,200]	26^{+106}_{-4}	kpc
Velocity dispersion	σ_0^*	[50,400]	108^{+77}_{-54}	km s ⁻¹

^(a) All parameters have uniform priors in the given range.

^(b) Offset with respect to BCG.

^(c) Position angle West of North.

^(d) The concentration is defined as $c_{200} = r_{200}/r_s$.

level, there are 5 sources in the NVSS map (all catalogued) and 3 in the SUMSS map (2 catalogued). Their positions and integrated fluxes, along with other properties, are listed in Table 3. The 833 MHz flux of source C has been estimated using `IMFIT` within the Common Astronomy Software Applications (CASA, McMullin et al. 2007).

From the *XMM-Newton* image we confirm that there are no X-ray point sources associated with the radio emission. Furthermore, sources A–D have no counterparts in the optical images, nor in the Near Infrared (NIR) from the 2 Micron All Sky Survey (2MASS, Strutskie et al. 2006) or the Mid Infrared (MIR) from the Wide-field Infrared Survey Explorer All Sky Survey (WISE, Wright et al. 2010), within their nominal position uncertainties. Source E has two plausible counterparts from the 2MASS and WISE (merged into one source) catalogs. Both are stars, and are also seen in our optical images. It is therefore likely that source E is a radio point source. However, the low resolution of the radio datasets does not allow us to rule out the possibility that the other sources might be dominated by radio point sources.

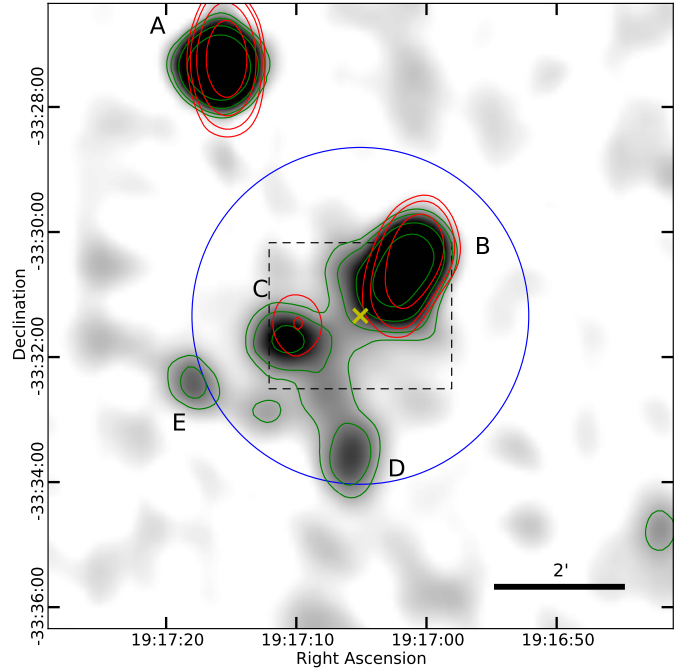


Fig. 3. NVSS 1.4 GHz radio intensity map around PLCK G004.5–19.5, with contours in green. SUMSS 843 MHz contours are shown in red. Both contour sets are in units of 3, 5, 10 and 20 times each background rms. The yellow cross shows the position of the BCG. The dashed black rectangle is the region shown in Figure 1 and the blue circle marks $r_{500} = 1.01$ Mpc. The black bar in the bottom right marks a scale of 2'.

We estimate the spectral index between 1.28 and 2.12 GHz (rest-frame) for sources A, B and C of $\alpha = 1.3, 0.9, 1.1$, respectively, where $F(\nu) = \nu^{-\alpha}$, and assume a spectral index of 1 for sources D and E. Using these spectral indices, we estimate the rest-frame 1.4 GHz power of each source, $P_{1.4}$, assuming that all the emission is produced at the cluster redshift. The power of sources A and B are of order $\sim 2 \times 10^{26}$ W Hz⁻¹, and those of sources C–E are of order $1\text{--}3 \times 10^{25}$ W Hz⁻¹ (see Table 3). In comparison, most clusters have radio powers $P_{1.4} \lesssim 10^{25}$ W Hz⁻¹.

(Feretti et al. 2012). The extremely large radio power of sources A and B hint that they may be contaminated by point sources. Higher resolution observations are required to clearly establish the nature of the diffuse radio emission associated with PLCK G004.5–19.5.

5. Discussion & Conclusions

We present optical confirmation of PLCK G004.5–19.5, one of the massive galaxy clusters recently discovered by the *Planck* satellite using the SZ effect. As expected, the optical image shows a red sequence of galaxies with a dominant BCG, plus a strong lensing giant arc, which is composed of two partially merged images of the background galaxy, and many more candidates for strong lensing images. Spectroscopy of 6 cluster members plus the giant arc show that the cluster is at $z = 0.516 \pm 0.002$ and that the arc is at $z_{\text{arc}} = 1.601$. With these data we have performed a strong lensing analysis, confirming a third image for the source producing the arc. We use LENS TOOL to obtain a mass model for the cluster, including the contribution from cluster galaxies, and estimate a median Einstein ring $r_E \simeq 185$ kpc (from an angular size $\theta_E(z_s = 1.6) \simeq 29''$). The mass enclosed within this radius is $M_E = (2.38 \pm 0.55) \times 10^{14} M_\odot$. Compared to the universal Einstein ring distribution recently derived by Zitrin et al. (2012), PLCK G004.5–19.5 is among the strongest gravitational lenses in the Universe. By integrating the 3-dimensional NFW profile we estimate $M_{500}^{SL} = 6.1_{-1.2}^{+2.3} \times 10^{14} M_\odot$. While this mass is significantly lower than estimates from SZ and X-ray observations, it involves an extrapolation over a factor of ~ 5 in radius from r_E to r_{500} . On the other hand, it could imply that on large ($\sim r_{500}$) scales, PLCK G004.5–19.5 does not follow an NFW profile.

Examination of archival radio data from NVSS at 1.4 GHz and SUMSS at 843 MHz suggest that PLCK G004.5–19.5 hosts a powerful radio halo, with extended emission detected at 3σ at 1.4 GHz on scales $\lesssim 1$ Mpc which could originate from an ongoing merger. We find no detectable point sources contributing significantly to the radio emission in the *XMM-Newton* or Gemini images, nor from archival observations in the NIR or MIR. Whether this emission is produced (mainly) by the cluster, however, requires confirmation with higher-resolution observations.

Acknowledgements. We thank Timo Anguita for help with the arc spectrum. CS acknowledges support from the European Research Council under FP7 grant number 279396 awarded to H. Hoekstra. CS and LFB have been supported by “Centro de Astrofísica FONDAP” 15010003, Centro BASAL-CATA, by

FONDECYT under project 1120676 and by ALMA-CONICYT under projects 31090002 and 31100003. JPH acknowledges support from NASA ADAP grant number NNX11AJ48G.

This research has made use of the VizieR catalogue access tool, CDS, Strasbourg, France. The original description of the VizieR service was published in A&AS 143, 23.

References

- Abazajian, K. N., Adelman-McCarthy, J. K., Agüeros, M. A., et al., 2009, *ApJ*, 182, 543
- Benítez, N., 2000, *ApJ*, 536, 571
- Benson, B. A., de Haan, T., Dudley, J. P., et al., 2013, *ApJ*, 763, 147
- Bertin, E., & Arnouts, S., 1996, *A&AS*, 317, 393
- Bertin, E., Mellier, Y., Radovich, M., et al., 2002, *ASPC*, 281, 228
- Bertin, E., 2012, *ASPC*, 461, 263
- Blanton, M. R., Hogg, D. W., Bahcall, N. A., et al., 2003, *ApJ*, 592, 819
- Condon, J. J., Cotton, W. D., Greisen, E. W., et al., 1998, *AJ*, 115, 1693
- Feretti, L., Giovannini, G., Govoni, F., & Murgia, M., 2012, *Astron. Astrophys. Rev.*, 20, 54
- Hao, J., McKay, T. A., Koester, B. P., et al., 2010, *ApJS*, 191, 254
- Hasselfield, M., Hilton, M., Marriage, T. A., et al., 2013, [arXiv:1301.0816](https://arxiv.org/abs/1301.0816)
- Jullo, E., Kneib, J.-P., Limousin, M., et al., 2007, *New J. Phys.*, 9, 447
- Kassiola, A., & Kovner, I., 1993, *ApJ*, 417, 450
- Kneib, J.-P., 1993, PhD Thesis, Univ. Paul Sabatier, Toulouse
- Kneib, J.-P., Ellis, R. S., Smail, I., Couch, W. J., & Sharples, R. M., 1996, *ApJ*, 471, 643
- Kneib, J.-P., & Natarajan, P., 2011, *ARA&A*, 19, 47
- Kurtz, M. J., & Mink, D. J., 1998, *PASP*, 110, 934
- Limousin, M., Morandi, A., Sereno, M., et al., 2012, [arXiv:1210.3067](https://arxiv.org/abs/1210.3067)
- Marriage, T. A., Acquaviva, V., Ade, P. A. R., et al., 2011, *ApJ*, 737, 61
- Mauch, T., Murphy, T., Buttery, H. J., et al., 2003, *MNRAS*, 342, 1117
- McDonald, M., Bayliss, M., Benson, B. A., et al., 2012, *Nature*, 488, 349
- McMullin, J. P., Waters, B., Schiebel, D., Young, W., & Golap, K., 2007, *Astronomical Data Analysis Software and Systems XVI*
- Menanteau, F., González, J., Juin, J.-B., et al., 2010a, *ApJ*, 723, 1523
- Menanteau, F., Hughes, J. P., Barrientos, L. F., et al., 2010b, *ApJS*, 191, 340
- Menanteau, F., Hughes, J. P., Sifón, C., et al., 2012, *ApJ*, 748, 7
- Meneghetti, M., Fedeli, C., Zitrin, A., et al., 2011, *A&A*, 530, A17
- Morandi, A., Pedersen, K., & Limousin, M., 2010, *ApJ*, 713, 491
- Navarro, J. F., Frenk, C. S., & White, S. D. M., 1995, *MNRAS*, 275, 56
- Ochsenbein, F., Bauer, P., & Marcout, J., 2000, *A&AS*, 143, 23
- Planck Collaboration, 2011a, *A&A*, 536, A8
- Planck Collaboration, 2011b, *A&A*, 536, A9
- Planck Collaboration, 2011c, *A&A*, 536, A11
- Planck Collaboration, 2013, [arXiv:1303.5089](https://arxiv.org/abs/1303.5089)
- Reichardt, C. L., Stalder, B., Bleem, L. E., et al., 2013, *ApJ*, 763, 127
- Schechter, P. L., 1976, *ApJ*, 203, 297
- Sifón, C., Menanteau, F., Hasselfield, M., et al., 2012, [arXiv:1201.0991](https://arxiv.org/abs/1201.0991)
- Strutskie, M. F., Cutri, R. M., Stiening, R., et al., 2006, *AJ*, 131, 1163
- Sunyaev, R. A., & Zel’dovich, Y. B., 1972, *Comm. Astrophys. Space Phys.*, 4, 173
- Williamson, R., Benson, B. A., High, F. W., et al., 2011, *ApJ*, 738, 139
- Wright, E. L., Eisenhardt, P. R. M., Mainzer, A. K., et al., 2010, *AJ*, 140, 1868
- Zitrin, A., Broadhurst, T., Bartelmann, M., et al., 2012, *MNRAS*, 423, 2308